Memory-induced excitability in optical cavities

B. Braeckeveldt,[1,*] K. J. H. Peters,[2] B. Verdonschot,[2,†] B. Maes,[1] and S. R. K. Rodriguez[2,†]

[1]*Micro- and Nanophotonic Materials Group, Research Institute for Materials Science and Engineering, University of Mons, 20 Place du Parc, Mons B-7000, Belgium*

[2]*Center for Nanophotonics, AMOLF, Science Park 104, 1098 XG Amsterdam, The Netherlands*

(Received 13 November 2023; revised 18 February 2024; accepted 25 February 2024; published 2 April 2024)

Neurons and other excitable systems can release energy suddenly given a small stimulus. Excitability has recently drawn increasing interest in optics, as it is key to realize all-optical artificial neurons enabling speed-of-light information processing. However, the realization of all-optical excitable units and networks remains challenging. Here we demonstrate how laser-driven optical cavities with memory in their nonlinear response can sustain excitability beyond the constraints of memoryless systems. First we demonstrate different classes of excitability and spiking, and their control in a single cavity with memory. This single-cavity excitability is limited to a narrow range of memory times commensurate with the linear dissipation time. To overcome this limitation, we explore coupled cavities with memory. We demonstrate that this system can exhibit excitability for arbitrarily long memory times, even when the intercavity coupling rate is smaller than the dissipation rate. Our coupled-cavity system also sustains spike trains—a hallmark of neurons—that spontaneously break mirror symmetry. Our predictions can be readily tested in thermo-optical cavities, where thermal dynamics effectively give memory to the nonlinear optical response. The huge separation between thermal and optical timescales in such cavities is promising for the realization of artificial neurons that can self-organize to the edge of a phase transition, like many biological systems do.

DOI: 10.1103/PhysRevResearch.6.023008

I. INTRODUCTION

The human brain can process information with an energy efficiency that far exceeds that of digital computers. This recognition is motivating the development of brain-inspired hardware to overcome major bottlenecks in computing [1–7]. Key to the success of this development is the realization of artificial neurons (ANs) which, like neurons in the brain, can fire information-rich energy spikes in response to small stimuli. This essential ability of neurons or ANs to release energy suddenly, in the form of spikes, is known as excitability [8].

ANs have been proposed and demonstrated on a variety of platforms [9–25]. Most state-of-the-art ANs process electrical or optical signals, and they can be made of ferroelectric [26–29], phase change [30–32], two-dimensional [33,34], or organic [35,36] materials, to name a few examples. A nonlinear response is key to excitability, and hence to the realization of ANs. Many efforts have therefore concentrated on the electrical domain, where strong nonlinearities enable low-power excitability. However, recent progress in the development of highly nonlinear photonic systems [37–41] is making these systems increasingly attractive for the realization of low-power ANs. Photonic systems offer excitability at unrivalled speed, but this is not enough to mimic the brain. The brain also embraces slow dynamics to realize its remarkable information processing capability. More precisely, the coupling of slow and fast dynamical variables grants the brain an ability to self-organize to the edge of a phase transition [42–48], where information processing is thought to be optimal and robust to parameter changes [45,49–53]. Hence, embracing the coupling of slow and fast variables is also important for the realization of ANs and brain-inspired computation.

In this manuscript we demonstrate the emergence of excitability, and its characteristics, in laser-driven optical cavities with memory in their nonlinear response. Like neurons and other biological systems, our cavities rely on the coupling of slow and fast variables to realize excitability across a wide range of timescales. Moreover, our cavities can emit a sequence of intensity spikes akin to "spike trains." In the brain, such spike trains encode information [20,54–58] in both the amplitude and separation of the spikes. While our work is purely theoretical and numerical, the system and parameter range we study can be readily realized using state-of-the-art thermo-optical cavities [10,13,59–62].

This manuscript is organized as follows. In Sec. II we introduce the model for a single laser-driven cavity with memory in its nonlinear response. We demonstrate different classes of excitability and spiking in such a cavity, their connection to limit cycles, and the limited parameter range over which excitability can be achieved. In Sec. III we demonstrate how to overcome the limitations of single cavities using coupled

*bertrand.braeckeveldt@umons.ac.be
†s.rodriguez@amolf.nl

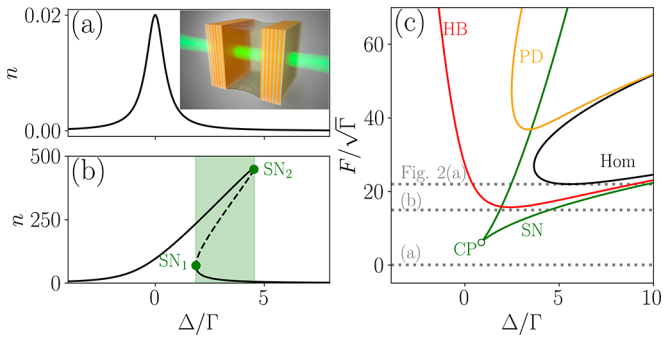

FIG. 1. (a) Intensity $n = |\alpha|^2$ vs detuning Δ referenced to the dissipation rate Γ for a laser amplitude $F = 0.1\sqrt{\Gamma}$. Inset: Illustration of an oil-filled cavity described by Eq. (1). (b) n vs Δ/Γ for $F = 15\sqrt{\Gamma}$. Solid (dashed) curves correspond to stable (unstable) solutions. The two saddle-node bifurcations (SN_i) are indicated by green dots. Green shaded area indicates the region of bistability. (c) Bifurcations in the (Δ, F) plane. Solid curves correspond to Hopf bifurcations (HB, red), period doubling bifurcations (PD, orange), homoclinic bifurcations (Hom, black), and saddle-node bifurcations (SN, green). The open circle indicates a cusp (CP). Dashed gray lines indicate the laser amplitudes studied in Figs. 1(a) and 1(b), and Fig. 2(a). Model parameters: $\Gamma = 1$, $\kappa_L = \Gamma/2$, $U = \Gamma/100$, $\tau = \Gamma^{-1}$, $D = 0$.

cavities. We explore how the coupling strength between the cavities, the memory time, and the laser noise impact the excitability of the coupled cavities. We show the existence of excitability for arbitrarily long memory times and the emergence of spike trains that spontaneously break the mirror symmetry of the coupled-cavity system. Finally, in Sec. IV we provide conclusions and perspectives of our work.

II. SINGLE-CAVITY EXCITABILITY

A. The model

Consider a coherently driven single-mode resonator with memory in its nonlinear response. For concreteness, we will refer to a laser-driven plano-concave Fabry-Perot cavity filled with oil, as illustrated in the inset of Fig. 1(a) and experimentally studied in Refs. [61,62]. However, the system we envisage can also be realized using ring resonators [63–65], whispering-gallery-mode resonators [66], photonic crystal cavities [67–70], and plasmonic particles [71], for example. All these resonators sustain a thermo-optical nonlinearity that makes the optical response noninstantaneous and leads to memory effects.

The cavity has resonance frequency ω_0, intrinsic loss rate γ, and nonlinearity of strength U. The input-output rates through the "left" and "right" mirror are κ_L and κ_R. A laser with frequency ω and amplitude F drives the cavity from the left. In a frame rotating at ω, the intracavity light field α follows

$$i\dot{\alpha}(t) = \left[-\Delta - i\frac{\Gamma}{2} + U\int_0^t ds\, K(t-s)|\alpha(s)|^2\right]\alpha(t) + i\sqrt{\kappa_L}F + \frac{D}{\sqrt{2}}[\xi(t) + i\zeta(t)]. \quad (1)$$

$\Delta = \omega - \omega_0$ is the laser-cavity detuning, and $\Gamma = \gamma + \kappa_L + \kappa_R$ is the total loss rate. The term with the integral represents the noninstantaneous nonlinearity. For a thermo-optical nonlinearity as in our system, the memory kernel is $K(t) = \exp(-t/\tau)/\tau$. The thermal relaxation time or memory time τ roughly determines how long the past exerts an influence on the system. The stochastic term $D[\xi(t) + i\zeta(t)]/\sqrt{2}$ accounts for Gaussian white noise with variance D^2 in the laser amplitude and phase. The noise components $\xi(t)$, $\zeta(t)$ each have zero mean [i.e., $\langle\xi(t)\rangle = \langle\zeta(t)\rangle = 0$] and are δ-correlated in time with unit variance [i.e., $\langle\xi(t)\xi(t+t')\rangle = \langle\zeta(t)\zeta(t+t')\rangle = \delta(t')$]. Moreover, $\xi(t)$ and $\zeta(t)$ are mutually uncorrelated [i.e., $\langle\xi(t)\zeta(t+t')\rangle = 0$].

Since the kernel $K(t)$ is integrable, we can rewrite the integrodifferential Eq. (1) as a set of ordinary differential equations, which are convenient for numerical integration and continuation. Writing $\alpha = u + iv$ and $w = U\int_0^t ds\, K(t-s)|\alpha(s)|^2$, we obtain the following equations for real valued variables:

$$\begin{aligned}
\dot{u}(t) &= -\frac{\Gamma}{2}u(t) + [w(t) - \Delta]v(t) + \sqrt{\kappa_L}F + \frac{D}{\sqrt{2}}\xi,\\
\dot{v}(t) &= -\frac{\Gamma}{2}v(t) - [w(t) - \Delta]u(t) + \frac{D}{\sqrt{2}}\zeta,\\
\dot{w}(t) &= \{U[u^2(t) + v^2(t)] - w(t)\}/\tau. \quad (2)
\end{aligned}$$

In the following we present solutions to this set of equations. For analyzing fixed points and their bifurcations under parameter continuations, we solve the deterministic equations using the software package AUTO-07P [72]. For analyzing dynamics, we numerically integrate the stochastic equations using a homemade solver in PYTHON.

B. Fixed points and bifurcations

First we consider the fixed points of Eq. (2) for various driving conditions and without noise ($D = 0$). Equation (2) has the form $\dot{\boldsymbol{x}} = \boldsymbol{f}(\boldsymbol{x})$, with $\boldsymbol{x} = (u, v, w)^\intercal$. The fixed points satisfy $\boldsymbol{f}(\boldsymbol{x}) = 0$, and their stability is determined by the eigenvalues of the Jacobian of $\boldsymbol{f}$. We distinguish three types of fixed points. (1) Node: All eigenvalues are real and of the same sign. A node is stable (unstable) when all eigenvalues are negative (positive). (2) Focus: There is at least one pair of complex conjugate eigenvalues. A focus is stable when the real part of all eigenvalues is negative, and it is unstable otherwise. (3) Saddle: There is at least one real positive and one real negative eigenvalue. A saddle is always unstable.

Figure 1(a) shows the intensity $n = |\alpha|^2 = u^2 + v^2$, or intracavity photon number, versus detuning for $F = 0.1\sqrt{\Gamma}$. For this small driving amplitude, n is small, the nonlinearity is negligible, and the spectral line shape resembles the Lorentzian of a linear cavity. In contrast, for a large driving amplitude $F = 15\sqrt{\Gamma}$, the line shape is tilted as Fig. 1(b) shows. This results in a detuning range with three fixed points, of which two are stable: optical bistability. The bistable region is enclosed by two saddle-node bifurcations (SN), at which a stable point collides with a saddle and disappears [73]. The SN bifurcations are also shown in Fig. 1(c), now as a function of F and Δ. They are the two green curves that meet tangentially

at a cusp (CP). The region enclosed by the SN bifurcations is the bistability region.

The locations of the cusp and the saddle nodes, as well as the optical bistability, are the same for our thermo-optical cavity and a Kerr nonlinear cavity where the nonlinearity is instantaneous. Indeed, at equilibrium, $\dot{w} = 0$ leading to $w = Un$, as for an instantaneous nonlinearity. However, the noninstantaneous nonlinearity leads to other types of dynamical state bifurcations absent in the instantaneous case. These bifurcations are due to the coupling of light to another degree of freedom, namely, w, which gives memory to the optical response and can result in instabilities. In particular, Fig. 1(c) indicates Hopf (red curve), period-doubling (yellow curve), and homoclinic (black curve) bifurcations, from which more complex dynamics emerge.

C. Limit cycles and excitability

Figure 2(a) shows the intensity as a function of detuning for a large driving amplitude, $F = 22\sqrt{\Gamma}$, indicated in Fig. 1(c). The points labeled $HB_{1,2}$ are Hopf bifurcations, where a focus changes stability via a pair of purely imaginary eigenvalues [73]. Crossing a Hopf bifurcation leads to a limit cycle—an isolated closed orbit in phase space. If the limit cycle is stable, self-sustained oscillations emerge. Figure 2(a) shows the maximum values of n of these self-sustained oscillations as solid red curves. Figure 2(a) also shows that as the detuning increases from HB_1 to the open circle labeled Hom_1, the limit cycle amplitude grows. The point (Hom_1) is known as a homoclinic bifurcation [73]. Approaching Hom_1, the period of the limit cycle diverges as Fig. 2(b) shows; the system spends more and more time near the saddle.

To illustrate how the limit cycle is transformed across the homoclinic bifurcation, Figs. 2(c)–2(e) show the phase portrait of the system at the detunings indicated by the dashed gray lines in Figs. 2(a) and 2(b). All three panels display three fixed points: one stable focus (blue dot), a saddle (gray dot), and an unstable focus (red dot). For a detuning far from the homoclinic bifurcation, Fig. 2(c) shows that trajectories starting near the unstable focus spiral outwards and converge to the limit cycle displayed in red. The system then remains on the limit cycle and self-oscillates indefinitely. Next, for a detuning exactly at the homoclinic bifurcation, a homoclinic orbit is formed: an orbit from the saddle to itself in an infinite time. This situation is depicted in Fig. 2(d), where we observe that the limit cycle has collided with the saddle to form a homoclinic orbit (red curve). The collision destroys the limit cycle. Thus there are no self-sustained oscillations between Hom_1 and Hom_2, even if the unstable focus remains. Figure 2(e) shows that, indeed, no limit cycle exists for $\Delta/\Gamma = 5.5$. Trajectories starting near the unstable focus spiral outwards until reaching the saddle and then spiral towards the stable focus. For greater detunings than the ones considered in Figs. 2(c)–2(e), the point Hom_2 is reached. This leads to a new limit cycle from another homoclinic bifurcation.

The above results demonstrate that, unlike for a single-mode cavity with instantaneous nonlinearity [74–82], a single-mode cavity with noninstantaneous nonlinearity can exhibit self-sustained intensity oscillations due to the existence of stable limit cycles. Such limit cycles are precursors

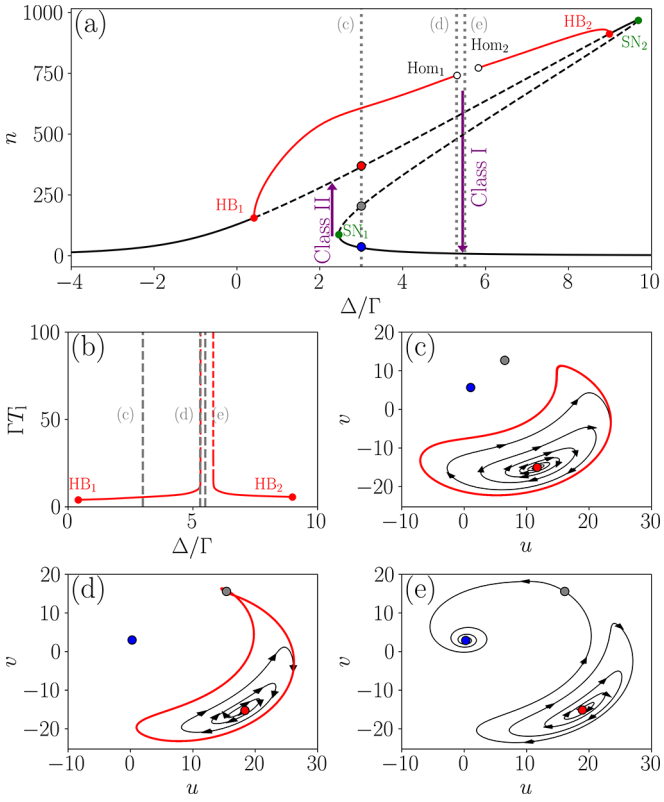

FIG. 2. (a) Intensity n as a function of Δ/Γ for $F = 22\sqrt{\Gamma}$. Solid (dashed) black curves correspond to stable (unstable) fixed points. Green and red dots indicate saddle-node (SN_i) and Hopf (HB_i) bifurcations, respectively. Red solid curves show the maximum n of limit cycle oscillations. Open black circle indicates homoclinic bifurcations (Hom_i). Purple arrows indicate transition directions with associated classes shown in Fig. 3. (b) Period of the limit cycle oscillations, T_l, as function of Δ/Γ. (c), (d), (e) Phase portraits at the detunings indicated by the dashed gray lines in (b). Dots indicate fixed points, with blue, red, and gray corresponding to stable focus, unstable focus, and saddle, respectively. Black curves show orbits with arrows indicating the direction. Red curves show stable limit cycles. Model parameters are as in Fig. 1, with $\Delta = 3\Gamma$, $\Delta = 5.3\Gamma$, and $\Delta = 5.5\Gamma$ in (c), (d), and (e), respectively.

for excitability—the hallmark of neurons. When a large-amplitude limit cycle is sufficiently close to an unstable focus, the system can transition between the stable focus (stationary state) and the unstable focus associated with the stable limit cycle; this transition results in a spike. It is precisely this ability of the system to release energy suddenly, in the form of spikes, which lies at the heart of excitability. The excitability of the system can be controlled via the parameter which makes the system transition from the resting to the spiking state, such as the detuning in this case.

Different classes of excitability and spiking can be distinguished. The classification is based on the evolution of the limit cycle period T_l (spiking state) versus the free parameter [8] [detuning in Fig. 2(a)]. Class I: the transition between the resting state and the spiking state is accompanied by a continuous evolution of the oscillation frequency ($1/T_l$). The oscillation period diverges at the transition. Class II: the frequency is discontinuous at the transition and is relatively

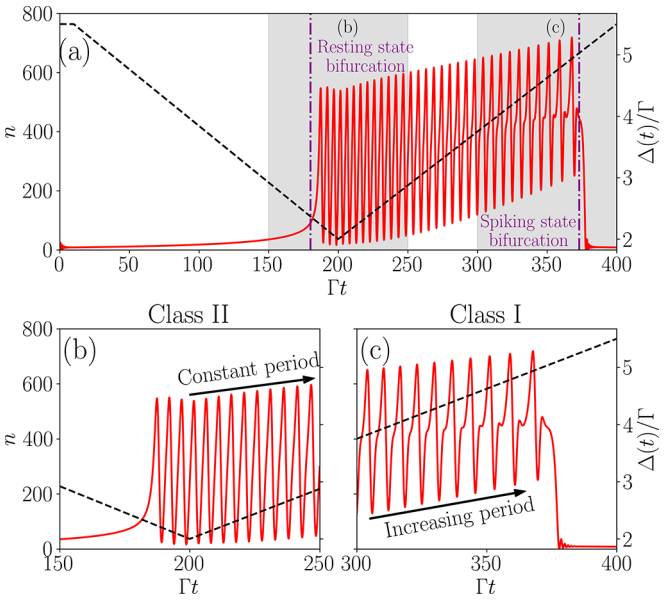

FIG. 3. n (solid red curve, left vertical axis) and detuning Δ/Γ (dashed black line, right vertical axis) vs time Γt. (a) Shaded areas correspond to the close-up views (b) and (c) of the transition from resting to spiking states, or vice versa, located by dashed-dotted vertical purple lines. (b) Zoom in on the resting state bifurcation corresponding to class-II excitability in Fig. 2(a). (c) Zoom in on the spiking state bifurcation associated with class-I spiking in Fig. 2(a). Model parameter values are as in Fig. 2(a). The detuning varies between $\Delta = 5.5\Gamma$ and $\Delta = 2.2\Gamma$.

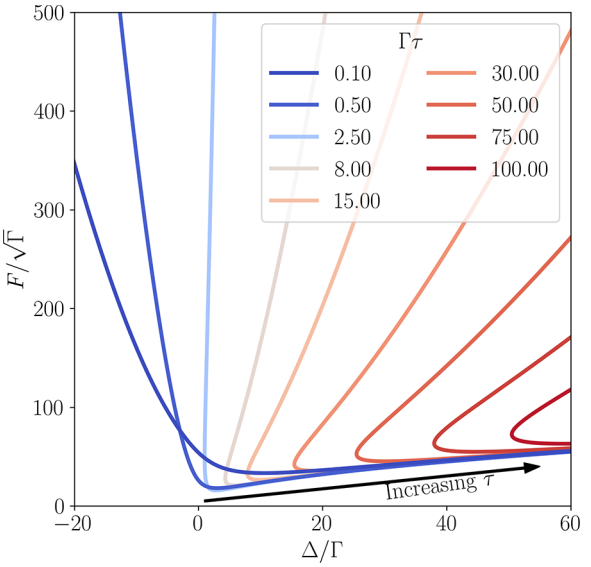

FIG. 4. Hopf bifurcation curves for a single cavity in the (Δ, F) plane for variable memory time τ. Model parameters are as in Fig. 1(c).

insensitive to changes in the free parameter. The frequency evolution from the resting state to the spiking state defines the class of excitability, whereas the reverse transition (from spiking to resting) corresponds to the class of spiking. Next, we illustrate how both class-II excitability and class-I spiking can be realized in our thermo-optical cavity.

Figure 3(a) shows the intensity $n(t)$ when the detuning Δ is ramped at fixed driving amplitude $F = 22\sqrt{\Gamma}$, as in Fig. 2. For $\Delta = 5.5\Gamma$, the system is in a resting state (stable focus) corresponding to the low-n branch of Fig. 2(a). For smaller Δ, this state undergoes a saddle-node bifurcation [SN_1 in Fig. 2(a)] when it collides with the saddle. After this bifurcation, the system is forced to enter the spiking state associated with the unstable focus. Thus, the system transitions from a zero-frequency resting state to a near-constant-frequency spiking state, as displayed in Fig. 3(b); this corresponds to class-II excitability [8]. The corresponding transition is represented by the upward-pointing arrow in Fig. 2(a).

Once the system is in the oscillatory state, the unstable focus undergoes a homoclinic bifurcation when the detuning is increased. Homoclinic bifurcations are associated with divergence of the oscillation period [see Fig. 2(b)]. Thus, during the transition from the spiking to the resting state in Fig. 3(c), the oscillation period increases just before the transition. The corresponding transition is represented by the downward-pointing arrow in Fig. 2(a), and it is associated with class-I spiking [8]. Therefore, the spiking state can be turned on and off via the saddle-node and the homoclinic bifurcation, respectively. The existence of such a spiking state, and the ability to control it (via the detuning in our case), is crucial to the realization of an AN. Like biological neurons, ANs can encode information in both the amplitude of the spikes and interspike time intervals. Thus, cavities with memory in the nonlinear response can in principle be used as building blocks of more complex systems (artificial neural networks) performing neuromorphic computation. However, the single-cavity system presents important limitations discussed next.

D. Limitations due to the memory time

We have so far considered a single value of the memory time: $\tau = \Gamma^{-1}$. In Fig. 4 we illustrate the effect of increasing τ on the Hopf bifurcations. The bifurcations shift to larger Δ/Γ as τ increases. This poses a major obstacle for observing, and harnessing, excitable dynamics in a single-mode cavity. The single-mode description we have made is only valid when the mode under study is well isolated, spectrally and spatially, from all other modes in the cavity. This condition can only be satisfied within a limited frequency range, which is typically less than a few tens of resonance linewidths. Consequently, memory times larger than $\Gamma\tau \simeq 30$ would require an unfeasible separation of cavity modes to remain in the single-mode limit. Therefore, the possibility to realize limit cycles and excitable dynamics in a single-mode cavity with noninstantaneous nonlinearity seems to be limited to relatively small values of τ. Consequently, systems with typical thermo-optical nonlinearity with $\tau \sim 10^6\Gamma^{-1}$ [61,62,83] would be unsuitable for verifying our predictions. A solution to this problem is presented in the next section.

While memory-induced excitability in single-mode cavities may be very challenging, other systems with shorter memory times could be considered. For instance, in exciton-polariton systems it is well known that an exciton reservoir can be created even under coherent driving [39,84–88]. Alternatively, dark excitons can be nonresonantly injected

simultaneously with coherent driving of polaritons [89]. It turns out that, in both cases, excitons act in a way that is mathematically equivalent to a thermo-optical nonlinearity. They effectively grant memory to the polariton response, albeit on much shorter timescales. The resulting set of equations for the system of polaritons coupled to excitons are indeed very similar to Eq. (2), with the decay time of excitons acting as a memory time. Based on parameters found in the literature [87], we expect such a system to present a memory time $\Gamma\tau \simeq 10$. Consequently, polariton-exciton interactions may lead to Hopf and homoclinic bifurcations on short timescales of tens to hundreds of picoseconds. To the best of our knowledge, the effects of these bifurcations have not been observed in polariton systems. We expect this prediction to stimulate efforts in that direction. Note that polariton systems have, in addition to a noninstantaneous nonlinearity due to polariton-exciton interactions, an instantaneous nonlinearity due to polariton-polariton interactions. Moreover, the relative strength of polariton-exciton and polariton-polariton interactions may be controlled via the configuration details, such as the exciton fraction, which depends on the frequency detuning between the laser and the exciton resonance. All these ingredients make up for a much richer system than the one we have considered. It is a system that deserves a more detailed analysis of its bifurcations and nonlinear behavior, which is beyond the scope of this manuscript.

III. EXCITABILITY OF COUPLED CAVITIES

A. The model

We propose to overcome the aforementioned limitations of a single cavity by using two identical cavities linearly coupled with strength J. Coupled-cavity systems can be realized in various platforms, such as photonic crystals [90,91], whispering-gallery-mode resonators [92], etched semiconductors [93,94], and open-access Fabry-Pérot microcavities with one mirror structured via focused-ion-beam milling [95] or laser writing [96,97]. Important for our approach is that each cavity can be addressed independently and that fluctuations in the driving fields are mutually uncorrelated. Fulfilling this requirement is easy with the systems cited above but hard with systems of stacked cavities [98], which are typically driven by the same laser beam.

A key ingredient of the coupled-cavity system we propose is memory in its nonlinear response. Memory effects can be achieved, for example, by inserting oil in open-access Fabry-Pérot microcavities, as it was done for single cavities in Refs. [61,62]. The considered coupled system is described by the set of equations for real valued variables:

$$\begin{aligned}
\dot{u}_j &= -\frac{\Gamma}{2}u_j - (\Delta - w_j)v_j - Jv_{3-j} + \sqrt{\kappa_L}F_j + \frac{D}{\sqrt{2}}\xi_j,\\
\dot{v}_j &= -\frac{\Gamma}{2}v_j + (\Delta - w_j)u_j + Ju_{3-j} + \frac{D}{\sqrt{2}}\zeta_j,\\
\dot{w}_j &= \frac{U\left(u_j^2 + v_j^2\right) - w_j}{\tau},
\end{aligned} \tag{3}$$

with $j \in 1, 2$. The two cavities are deterministically driven with equal amplitude and phase, but the stochastic terms are independent, i.e.,

$$\begin{aligned}
\langle \xi_j(t)\zeta_k(t+t')\rangle &= 0 \quad j,k \in \{1,2\},\\
\langle \xi_j(t)\xi_k(t+t')\rangle &= \delta(t')\delta_{jk} \quad j,k \in \{1,2\}.
\end{aligned} \tag{4}$$

We focus on dispersive coupling $J \in \mathbb{R}^+$, which is typical of experimental systems [90,91,93,94,97,99]. For $J > \Gamma$ the spectrum comprises a symmetric ($\alpha_1 = \alpha_2$) and antisymmetric ($\alpha_1 = -\alpha_2$) superposition of the bare cavity modes, split by $2J$.

Even without memory ($\tau \to 0$), coupled cavities can sustain complex dynamics which have drawn great interest in recent years [93,99–110]. Hopf and homoclinic bifurcations and chaos [101,102,105,106], as well as excitability [108], have been numerically shown in the strong-coupling regime ($J > \Gamma$). In all those systems, limit cycles have a relatively short period $T_l \propto J^{-1} \sim$ ps limited by the high coupling rates of optical cavities. The subpicosecond time resolution needed to observe such oscillations has made their direct experimental observation and utilization impossible so far.

In the following we show that coupled cavities with noninstantaneous nonlinearity can overcome the limitations of both the single-cavity system with noninstantaneous nonlinearity, as well as those of coupled-cavity systems with instantaneous nonlinearity. In particular, we will show that limit cycles and excitability can be realized in systems with memory times τ much larger than the dissipation time Γ^{-1}.

B. Fixed points and bifurcations

Coupled cavities support fixed points absent in the single cavity. In Fig. 5(a) we plot the intensity in cavity 1 (n_1) versus Δ/Γ. We obtained this plot by solving Eq. (3) with constant driving amplitude ($F = 15.7\sqrt{\Gamma}$). Solutions are color coded as in the previous section. The black curves correspond to the symmetric solutions and behave similarly to the single cavity [see Fig. 1(b)] due to the symmetric driving. Between saddle-node bifurcations labeled $SN_{1,2}$, the coupled system exhibits three symmetric states, two of them being stable and one unstable. Asymmetric solutions [blue branches in Fig. 5(a)] are connected to the symmetric one via pitchfork bifurcations ($PB_{1,2}$), indicated by the blue dots in Fig. 5(a). The location of these bifurcations can be computed analytically (see Appendix C).

To illustrate the complex behavior appearing in the multistability region, Fig. 5(b) shows the fixed points in the (n_1, n_2) space for $\Delta = 1.5\Gamma$, color coded as indicated in the caption. Due to the mirror symmetry, the intensities in both cavities can be expected to be equal and therefore lie along the symmetry axis indicated by the dashed black line. This mirror symmetry can spontaneously break [91,111] and asymmetric solutions $n_1 \neq n_2$ emerge. Interestingly, limit cycles appear in asymmetric solutions as they undergo Hopf bifurcations ($HB_{1,2}$) represented by red dots. A stable limit cycle with a maximum intensity displayed via a short red line emerges from each of these bifurcations. Limit cycles disappear via homoclinic bifurcations ($Hom_{1,2}$) located with open circles. A zoom in on HB_1 and Hom_1 bifurcations [Fig. 5(a) main panel] is shown as an inset in Fig. 5(a).

Remarkably, all bifurcations in Fig. 5(a) correspond to a small coupling $J = 0.5\Gamma$ and large memory time $\tau = 100/\Gamma$.

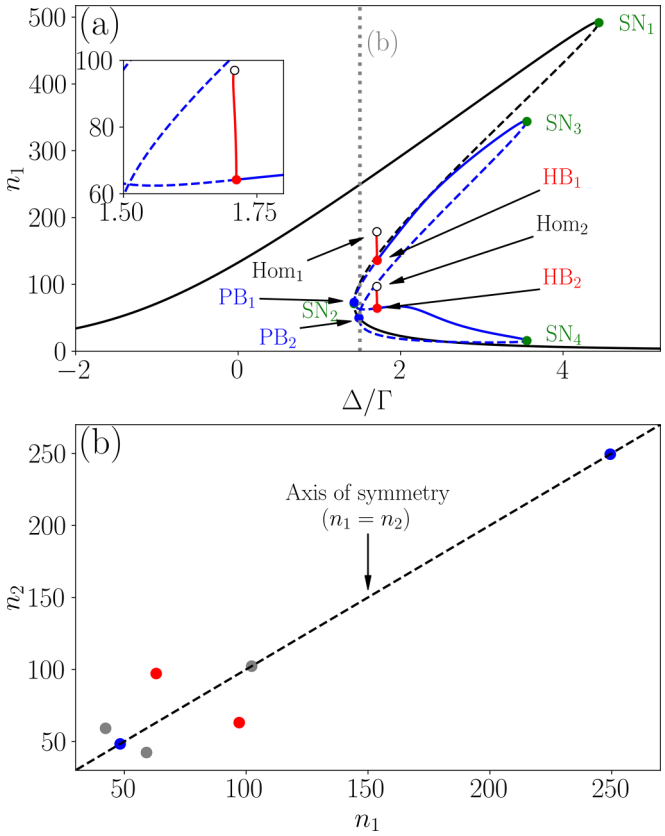

FIG. 5. (a) Bifurcation diagram of n_1 along the detuning Δ for coupled and symmetrically driven cavities. Solid (dashed) curves represent stable (unstable) fixed points with symmetric and asymmetric solutions in black and blue, respectively. Saddle-node (SN, green), Hopf (HB, red), homoclinic (Hom, black), and pitchfork (PB, blue) bifurcations are located with green, red, empty, and blue dots, respectively. Inset: Close-up view of Hopf (HB_1) and homoclinic (Hom_1) bifurcations in the main panel. The red solid curve represents the maximum intensity of the stable limit cycle. (b) Fixed points for a detuning $\Delta = 1.5\Gamma$ color coded as in Fig. 2. The dashed black line shows the axis of symmetry $n_1 = n_2$. Model parameters: $\Gamma = 1$, $U = \Gamma/100, \kappa_L = \Gamma/2, D = 0, J = 0.5\Gamma, F = 15.7\sqrt{\Gamma}, \tau = 100\Gamma^{-1}$.

This already shows that the limitations previously discussed are gone. Coupled cavities with noninstantaneous nonlinearity can sustain limit cycles for very long memory times, even when the coupling is weaker than the dissipation.

Figure 5(a) shows that Hopf bifurcations occur in the asymmetric branches, absent in the single-cavity system. To relate these results to single-cavity physics, let us assume excitation of the symmetric mode by setting $\alpha_1 = \alpha_2$ in Eq. (3). By considering steady states without noise ($D = 0$), one obtains

$$0 = \left[i(\Delta + J - U|\alpha_j|^2) - \frac{\Gamma}{2}\right]\alpha_j + \sqrt{\kappa_L}F, \tag{5}$$

with $j \in 1, 2$. The above equation is equivalent to that describing a single cavity, but with the detuning shifted by the coupling J. Taking the square modulus leads to a cubic equation in $n_j = |\alpha_j|^2$, which gives three possible symmetric solutions (see Appendix A). However, these symmetric solutions are not the only ones. Even under symmetric driving, asymmetric solutions emerge due to spontaneous symmetry breaking. One can show (see Appendix B) that the steady states generally satisfy

$$(n_1 - n_2)\left[U^2\left(n_1^2 + n_2^2 + n_1 n_2\right) - 2U(\Delta - J)(n_1 + n_2) + \frac{\Gamma^2}{4} + (\Delta - J)^2\right] = 0. \tag{6}$$

Equation (6) is the product of two terms, and it is therefore satisfied if at least one of them is zero. The first leads to symmetric solutions because it is zero for $n_1 = n_2$. Consequently, there is always at least one symmetric solution. The second term (in the square brackets) can cancel even for asymmetric solutions $n_1 \neq n_2$. These asymmetric solutions exist under the following conditions (see Appendix B):

$$\Delta \geqslant J + \frac{\sqrt{3}}{2}\Gamma, \tag{7a}$$

$$n_j \leqslant \frac{2(\Delta - J) + \sqrt{4(\Delta - J)^2 - 3\Gamma^2}}{3U}, \tag{7b}$$

$$n_j \geqslant \frac{2(\Delta - J) - \sqrt{4(\Delta - J)^2 - 3\Gamma^2}}{3U}. \tag{7c}$$

Due to the mirror symmetry of the system, asymmetric solutions always appear in pairs, with n_1 and n_2 symmetric around the axis $n_1 = n_2$ [Fig. 5(b)]. There can be 2, 4, 6, or 8 asymmetric solutions. Figure 5(a) and its inset show that, unlike the branches associated with the symmetric solutions, the asymmetric branches support Hopf and homoclinic bifurcations. Stable limit cycles exist in between these bifurcations and are therefore present for a small detuning range.

C. Limit cycles and excitability

The coupled-cavity system also displays class-I spiking and class-II excitability, as the system can transition from a symmetric stable focus to an asymmetric unstable focus associated with a stable limit cycle. To induce the symmetry breaking we need an initial slight asymmetry in the driving fields. We therefore define the driving amplitude imbalance between the two cavities $\rho = (F_1 - F_2)/(F_1 + F_2)$, and we vary this parameter to reveal excitable dynamics.

Figure 6(a) shows the time evolution of n_1 and n_2 when the driving imbalance ρ is ramped. We observe two transitions in the shaded areas of Fig. 6(a). The first transition, displayed in Fig. 6(b), shows the jump from a symmetric resting state to an asymmetric stable limit cycle (spiking state). The oscillation period goes from zero to a near-constant value and is therefore discontinuous and characteristic of class-II excitability. In contrast, the other transition presented in Fig. 6(c) shows that the intensities switch from an asymmetric stable limit cycle to a symmetric rest state. The transition is associated with a continuous increase of the oscillation period associated with class-I spiking. Again, the coupled system presents spiking dynamics that can be switched on or off. In contrast to the single cavity, the oscillatory state of the coupled cavities is triggered by varying the driving imbalance instead of the detuning.

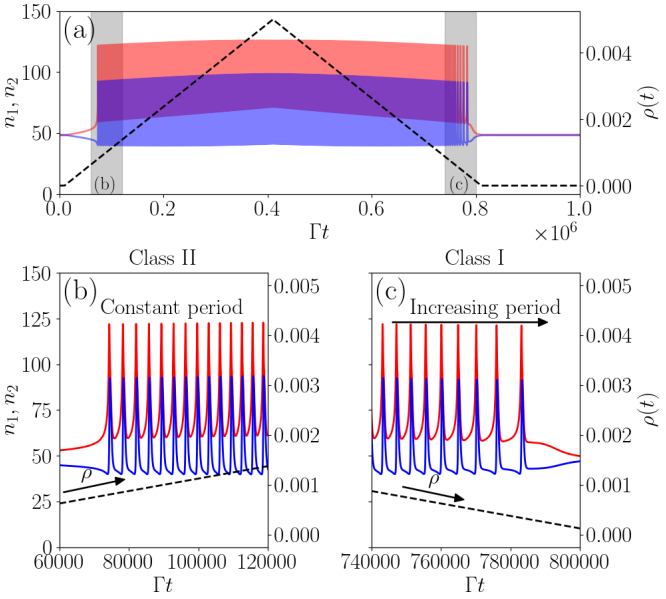

FIG. 6. n_1 (red curve, left vertical axis), n_2 (blue curve, left vertical axis), and power imbalance $\rho = (F_1 - F_2)/(F_1 + F_2)$ (dashed black line, right vertical axis) versus time Γt. (a) Shaded areas correspond to the close-up views in (b), (c). (b) Zoom in on the transition from resting to the spiking state associated with class-II excitability. (c) Zoom in on the transition from spiking to the resting state corresponding to class-I spiking. The average power $F = [F_1(t) + F_2(t)]/2$ is constant and equals $F = 15.7\sqrt{\Gamma}$. The detuning is $\Delta/\Gamma = 1.5$. Other model parameters are as in Fig. 5(a). The power imbalance ρ varies between 0 and 5×10^{-3}.

D. Persistence and accessibility of excitability

In Fig. 7 we investigate the role of the coupling on the existence of limit cycles in our coupled-cavity system. We fix all parameters, except J, to the values used in Fig. 5. The region where limit cycles exist is located between the solid and dash-dotted curves of the same color, delimiting Hopf and homoclinic bifurcations, respectively. Open circles indicate Bogdanov-Takens bifurcations, where saddle-node, homoclinic, and Hopf bifurcations intersect. For a weak coupling ($J = 0.5\Gamma$), oscillations occur in a narrow detuning range as we have seen in Fig. 5. Interestingly, these limit cycles persist for much smaller detuning values than in the single-cavity system, even though the memory time is relatively large. Previously, in Fig. 4 we showed that $\Gamma\tau = 100$ would require $\Delta > 50\Gamma$ to observe limit cycles in a single cavity. For such extremely large detunings, no experiment is likely to be well described by a single-mode model. In contrast, for coupled cavities and $\Gamma\tau = 100$, limit cycles appear around $\Delta \simeq 1.6\Gamma$, which is experimentally feasible.

As J increases, Hopf and homoclinic bifurcations shift to higher driving amplitudes and detuning. This can be expected by noting that Hopf bifurcations appear in asymmetric branches. We noted that these solutions appear for detunings satisfying Eq. (7a), leading to larger Δ for an increasing coupling J. Moreover, the intensities $n_{1,2}$ also increase according to Eqs. (7b) and (7c), which means large driving amplitudes $F/\sqrt{\Gamma}$ are needed. Nonetheless, even for the larger coupling $J = 2.5\Gamma$, the driving amplitude and detuning for limit cycles

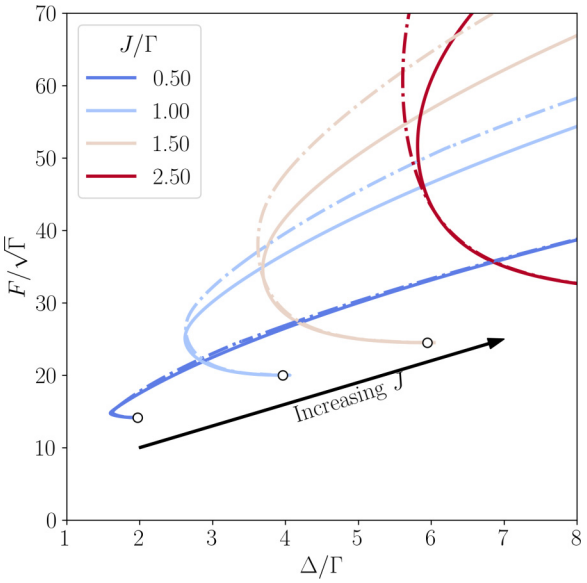

FIG. 7. Hopf (solid curves) and homoclinic (dash-dotted curves) bifurcations in the (Δ, F) space for various intercavity coupling strengths J. White dots indicate Bogdanov-Takens (BT) bifurcations. Model parameters are as in Fig. 5.

can still be achieved experimentally. For energy-efficient excitability, weak couplings J are better as they enable spiking activity with lower laser powers.

E. Excitability for arbitrarily long memory times

Figure 8 illustrates how the Hopf bifurcation in the asymmetric branch depends on the memory time τ. We use the same parameters as in Fig. 7, except that the coupling is now fixed at $J = 0.5\Gamma$ and τ varies. To avoid an overcrowded figure, we display Hopf and not homoclinic bifurcations. Open circles indicate Bogdanov-Takens bifurcations. For memory times $\Gamma\tau > 25$, the location of the Hopf bifurcation is not significantly influenced by τ as shown in Fig. 8(a). The homoclinic bifurcation behaves similarly as the Hopf bifurcation with the increase of the memory time. In Fig. 8(b) we provide a close-up view of the same curves, where we see that they all merge for $\Gamma\tau > 150$. Thanks to this limiting behavior for

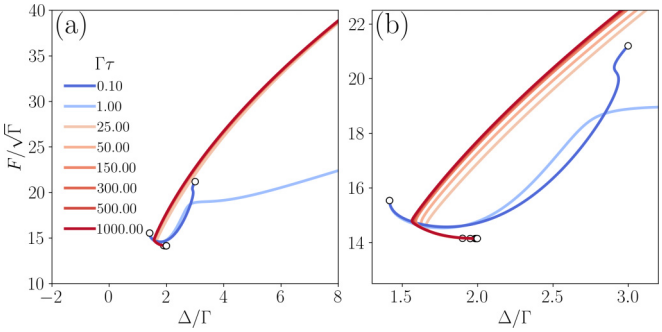

FIG. 8. (a) Hopf bifurcation on the asymmetric branches in the (Δ, F) space for various memory times τ when the coupling is $J = 0.5\Gamma$. (b) Close-up view on the limit behavior when $\Gamma\tau \gg 1$. Model parameters are as in Fig. 5.

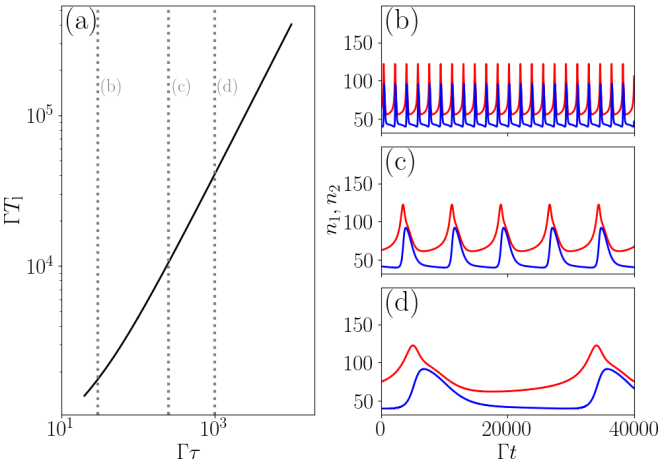

FIG. 9. (a) Limit cycle period T_l vs memory time τ, calculated via numerical continuation. Dotted lines indicate the memory times considered in (b)–(d). (b)–(d) n_1 (red) and n_2 (blue) vs time in a limit cycle regime for different memory times τ. (b) $\tau = 30\Gamma^{-1}$. (c) $\tau = 250\Gamma^{-1}$. (d) $\tau = 1000\Gamma^{-1}$. $F_1 = 15.72\sqrt{\Gamma}$, $F_2 = 15.68\sqrt{\Gamma}$. Other model parameters are as in Fig. 6.

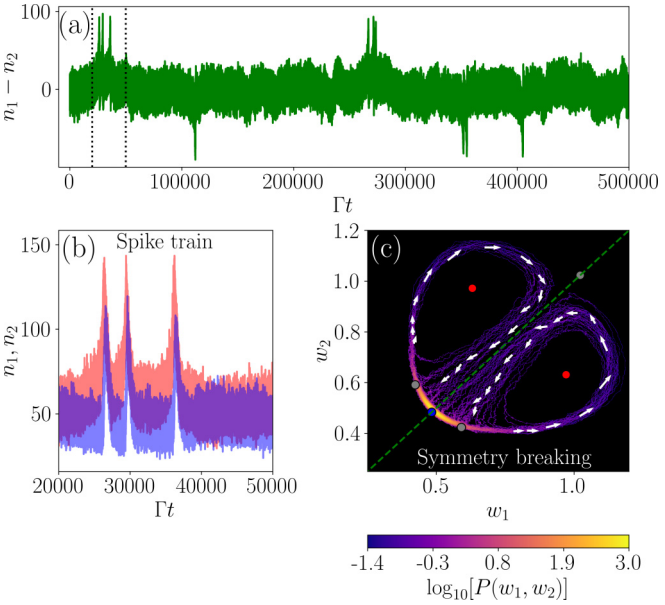

FIG. 10. (a) Intensity difference $n_1 - n_2$ vs time, for a standard deviation of the laser noise $D = 0.55\sqrt{\Gamma}$. Each spike represents an instance of spontaneous mirror symmetry breaking, whereby the intensity in one of the cavities substantially exceeds that in the other. (b) Zoom in on the first bursting event of (a) with n_1 in red and n_2 in blue. (c) Probability density function $P(w_1, w_2)$ computed from numerical time traces. Small white arrows indicate the rotation direction of each stable limit cycle. Dots represent fixed points color coded as in Fig. 2. The dashed green line shows the axis of symmetry ($w_1 = w_2$). Model parameters are as in Fig. 6, with $F = 15.7\sqrt{\Gamma}$ and $\rho = 0$.

$\Gamma\tau \gg 1$, effects of the Hopf bifurcation could be observed even in systems with extremely large memory times, such as the oil-filled cavities in Refs. [61,62].

When memory and dissipation times are commensurate ($\tau \sim \Gamma^{-1}$), the Hopf bifurcation curve has a different shape. As for a single cavity, the interplay of dissipation and memory effects leads to more complex dynamics, and many fixed points become unstable foci.

Next we demonstrate that increasing τ leads to proportionally longer limit cycles, thus enabling "slow firing." Via a modification of the memory time, the firing period can be tailored. The behavior we discuss is similar to spike frequency adaptation, also known as spike accommodation, observed in neurons [112]. Spike frequency adaptation is associated with a decrease in the frequency of spiking during an extended period of excitation. This frequency decrease is related to a slow recovery of the calcium-activated potassium channel responsible for the action potential [113].

Figure 9 illustrates how the period of the limit cycle depends on the memory time τ. Figure 9(a) shows an approximately linear relation between the limit cycle period T_l and τ. We note that this log-log scale curve is a continuation calculation (using AUTO-07P) along the memory time of the fixed point associated with the stable limit cycle. Figures 9(b), 9(c), and 9(d) correspond to $\Gamma\tau = 30$, 250, and 1000, respectively. Red and blue curves represent intensities in cavities 1 and 2, respectively. To set the system in the observed asymmetric self-oscillating states, we initialized our simulations close to the unstable focus associated with the stable limit cycle.

The results in Fig. 9 evidence that, unlike in previous systems (single cavity with noninstantaneous nonlinearity, and coupled cavities with instantaneous nonlinearity), limit cycles with periods unconstrained by J can emerge. These limit cycles can be realized for small couplings and small driving powers, as in Figs. 6 and 9, and for arbitrarily long memory times. Since both Hopf and homoclinic bifurcations shift to larger driving powers as the intercavity coupling increases (see Fig. 7), the laser power needed for excitability increases with the coupling strength. Consequently, weakly coupled cavities with long memory times are promising for the realization of low-power excitability. Moreover, the possibility to have coupled slow and fast variables (separated by many orders of magnitude in time) opens the possibility of self organization to the edge of a phase transition, as thought to occur in the brain [46,47].

F. Noise-induced spike trains

So far we have only considered the behavior of our system in the absence of noise. In this section we investigate how noise, in the laser amplitude and phase, results in asymmetric spike trains even when the deterministic driving is symmetric. Figure 10(a) shows the intensity imbalance in the two cavities, $n_1 - n_2$, versus time. The driving is symmetric on the two cavities, with amplitude $F = 15.7\sqrt{\Gamma}$. The detuning is $\Delta = 1.5\Gamma$, as in Fig. 6. Even though the standard deviation of the noise is the same for both cavities ($D = 0.55\sqrt{\Gamma}$), small asymmetries can be generated because the noise sources are independent. For this reason we mentioned at the beginning of this section that addressing each cavity with a different field and noise is important. Otherwise, spontaneous symmetry breaking cannot emerge. In the calculation we set $\Gamma\tau = 100$ to avoid unnecessarily long computation times associated with long memory times. However, in view of the already large

separation of timescales between Γ^{-1} and τ, qualitatively similar dynamics is expected for slower systems.

In Fig. 10(a) the system starts in a symmetric rest state, corresponding to the state at $t > 8\times10^5\Gamma^{-1}$ in Fig. 6. Then it suddenly and briefly transitions to symmetry-broken states associated with spiking as in Fig. 6(b). Figure 10(b) shows a close-up view of the interval containing the first three spikes in this particular trajectory, with n_1 and n_2 now plotted separately. Initially, the two intensities fluctuate around the same value, indicating symmetric behavior. Then the symmetry is broken during the spikes due to the random imbalance in the driving.

Symmetry breaking can also be observed in the (w_1, w_2) space by looking at the probability density function (PDF) $P(w_1, w_2)$ as in Fig. 10(c). The PDF is computed from eight trajectories of duration $5\times10^5/\Gamma$, each associated with 2×10^6 time steps. The probability is largest close to the symmetric stable focus indicated by the blue dot. The probability decreases approaching the two saddles (gray dots) close to the stable focus. When the system reaches a saddle, it undergoes a saddle-node bifurcation and initiates one of two limit cycles. The symmetry-broken states are associated with these limit cycles. The random fluctuations can then force the system to return to the stable focus. The transition from the symmetry-broken spiking states to the symmetric rest state can also be induced by a homoclinic bifurcation when the limit cycle swells and forms a homoclinic orbit.

In Fig. 10(c) we indicate the directions of the orbits around the two unstable foci with white arrows. There are two possible orbits because there are two symmetry-broken states (red dots) associated with spiking activity. Each of these states corresponds to a different sign of the power imbalance ρ. A positive ρ leads to n_1 larger than n_2, while the situation is reversed when ρ is negative. Here, the noise terms acting on each cavity are uncorrelated, leading to small imbalances on the total driving amplitudes. In other words, the combined noise terms effectively act as a fluctuating ρ. Thus, the imbalance ρ fluctuates between positive and negative values with equal probability, leading to spontaneous switching between both asymmetric spiking states. This enables the system to switch from one limit cycle to another, spontaneously. While spontaneous symmetry-breaking effects have been observed for localized modes [90,91,99,114–118], to the best of our knowledge they have never been observed for limit cycles as predicted in Fig. 10.

IV. CONCLUSIONS AND PERSPECTIVES

Cavities with memory in their nonlinear response, due, for example, to thermo-optical nonlinearities or excitonic effects, support self-sustained intensity oscillations under constant driving. These limit cycles play a crucial role in excitability, which is fundamental to the spiking behavior of neurons. We have observed that when memory and dissipation times are commensurate, a single-mode cavity can become excitable. The cavity exhibits Hopf and homoclinic bifurcations, corresponding to class-II excitability and class-I spiking, respectively. These effects can in principle also arise for longer memory times, but their experimental realization poses major technical challenges.

To expand the range of memory times over which spiking behavior can be practically realized, we proposed to couple two of the aforementioned cavities. We showed that this coupled system supports limit cycles, and consequently excitability, for arbitrarily long memory times. These limit cycles are furthermore associated with spontaneous breaking of mirror symmetry, and they enable spike trains akin to those observed in neurons to emerge. While coupled-cavity systems with instantaneous nonlinearity can also support limit cycles and excitability, our system with noninstantaneous nonlinearity enables these features to emerge for smaller intercavity coupling strengths and input powers. This smaller power requirement is promising for the realization of energy-efficient neuromorphic computing, assuming artificial neural networks can be made out of our cavities.

While we did not explicitly show it, our system can in principle be used as an artificial neuron. Indeed, excitability is the essential nonlinear dynamical property of neurons [8]. Information can be encoded in the amplitude of the spikes and their intervals. However, further research is needed to establish how optical cavities could be used as artificial neurons. We foresee technical challenges in the system realization, driving scheme, and in the protocols for encoding and decoding information.

Finally, we highlight that our discovery of excitability for arbitrarily long memory times is promising for technological realizations of a key feature of the brain: spiking behavior involving coupled slow and fast variables. Such slow-fast systems are among the most studied in the context of excitability (see, for example, [119]). The large separation of timescales is thought to underlie many of the remarkable computational properties of the brain [46,47]. Thus, our work opens the door to the development of all-optical artificial neural networks embracing slow-fast dynamics like those characterizing the brain. Assessing the cascadability [13,120] of our coupled-cavity system will be a crucial step towards the goal of using this system for computation.

ACKNOWLEDGMENTS

This work was supported by the Fonds pour la Formation à la Recherche dans l'Industrie et dans l'Agriculture (FRIA) and by the Fonds National de Recherche Scientifique (FNRS) in Belgium. Computational resources have been provided by the Consortium des Équipements de Calcul Intensif (CÉCI), funded by the FNRS under Grant No. 2.5020.11 and by the Walloon Region. This work is part of the research programme of the Netherlands Organization for Scientific Research (NWO). S.R.K.R. acknowledges an ERC Starting Grant, Project No. 852694.

APPENDIX A: SYMMETRIC FIXED POINTS

Here we show that the symmetrically driven cavities support symmetric fixed points similar to that of the single cavity. Neglecting noise, fixed points of the single cavity satisfy

$$0 = \left[i(\Delta - U|\alpha|^2) - \frac{\Gamma}{2} \right] \alpha + \sqrt{\kappa_L} F, \tag{A1}$$

which is clearly similar to Eq. (5), giving symmetric fixed points for the coupled system. The only difference is that, for coupled cavities, the detuning Δ is shifted by the coupling J.

By taking the modulus squared of both side of Eq. (5), one sees that fixed points are roots of a third-order polynomial in $n = |\alpha|^2$,

$$\mathcal{P}(n) \equiv U^2 n^3 - 2(\Delta + J)U n^2 - \left[(\Delta + J)^2 \frac{\Gamma^2}{4} + \right] n - \kappa_L |F|^2. \tag{A2}$$

As $n \in \mathbb{R}$, $\mathcal{P}$ has either one or three roots (in between saddle-node bifurcations).

APPENDIX B: RANGE OF PARAMETERS FOR ASYMMETRIC SOLUTIONS

Here we give the constraints for observing asymmetric solutions under symmetric driving. All fixed points of the coupled system satisfy

$$\left[i(\Delta - J - U|\alpha_1|^2) - \frac{\Gamma}{2}\right]\alpha_1 = \left[i(\Delta - J - U|\alpha_2|^2) - \frac{\Gamma}{2}\right]\alpha_2. \tag{B1}$$

Taking the modulus squared of both sides leads to Eq. (6). Here the equation involves the frequency $\Delta - J$ because we are interested in asymmetric modes. Asymmetric fixed points can not cancel the first parenthesis of Eq. (6) because $n_1 \neq n_2$ by definition of the asymmetry. Therefore the only possibility for asymmetric fixed points is that the second parenthesis [the one multiplied by $(n_1 - n_2)$] in Eq. (6) cancels. The beforementioned condition means that

$$U^2(n_1^2 + n_2^2 + n_1 n_2) - 2U(\Delta - J)(n_1 + n_2) + \frac{\Gamma^2}{4} + (\Delta - J)^2 = 0, \tag{B2}$$

which can be seen as a second-order polynomial in n_2 with roots

$$n_2 = \frac{-U n_1 + 2(\Delta - J)}{2U} \pm \frac{\sqrt{-3U^2 n_1^2 + 4U n_1(\Delta - J) - \Gamma^2}}{2U}. \tag{B3}$$

As $n_2 \in \mathbb{R}^+$, the square-root argument must be positive. This argument is a second-order polynomial in n_1 and is positive if n_1 lies between its roots:

$$n_1 = \frac{2(\Delta - J) \pm \sqrt{4(\Delta - J)^2 - 3\Gamma^2}}{3U}. \tag{B4}$$

These values are reals and positives as long as $\Delta \geqslant J + \sqrt{3}\Gamma/2$, which is the condition equation (7a). Thus n_2 in Eq. (B3) is real as long as n_1 is in between the roots Eq. (B4). Because n_1 and n_2 can be swapped in Eq. (B2), it leads to conditions equations (7b) and (7c).

APPENDIX C: PITCHFORK BIFURCATIONS

Pitchfork bifurcations are located at the intersections of symmetric and asymmetric solutions. Therefore fixed points associated with these bifurcations are roots of Eq. (B2) but also satisfy $n_1 = n_2 = n$. These two observations lead to

$$3U^2 n^2 - 4U(\Delta - J)n + \frac{\Gamma^2}{4} + (\Delta - J)^2 = 0. \tag{C1}$$

At the pitchfork bifurcations the intensity is

$$n_\pm = \frac{2(\Delta - J) \pm \sqrt{(\Delta - J)^2 - 3\Gamma^2/4}}{3U}. \tag{C2}$$

The input power corresponding to these intensities can be computed easily by injecting $n_\pm$ in the modulus square of Eq. (5).

[1] D. Ielmini and H.-S. P. Wong, In-memory computing with resistive switching devices, Nat. Electron. **1**, 333 (2018).

[2] C. Ríos, N. Youngblood, Z. Cheng, M. L. Gallo, W. H. P. Pernice, C. D. Wright, A. Sebastian, and H. Bhaskaran, In-memory computing on a photonic platform, Sci. Adv. **5**, eaau5759 (2019).

[3] A. Sebastian, M. Le Gallo, R. Khaddam-Aljameh, and E. Eleftheriou, Memory devices and applications for in-memory computing, Nat. Nanotechnol. **15**, 529 (2020).

[4] D. Marković, A. Mizrahi, D. Querlioz, and J. Grollier, Physics for neuromorphic computing, Nat. Rev. Phys. **2**, 499 (2020).

[5] B. J. Shastri, A. N. Tait, T. Ferreira de Lima, W. H. P. Pernice, H. Bhaskaran, C. D. Wright, and P. R. Prucnal, Photonics for artificial intelligence and neuromorphic computing, Nat. Photon. **15**, 102 (2021).

[6] D. V. Christensen, R. Dittmann, B. Linares-Barranco, A. Sebastian, M. L. Gallo, A. Redaelli, S. Slesazeck, T. Mikolajick, S. Spiga, S. Menzel, I. Valov, G. Milano, C. Ricciardi, S.-J. Liang, F. Miao, M. Lanza, T. J. Quill, S. T. Keene, A. Salleo, J. Grollier *et al.*, 2022 roadmap on neuromorphic computing and engineering, Neuromorph. Comput. Eng. **2**, 022501 (2022).

[7] M. Rao, H. Tang, J. Wu, W. Song, M. Zhang, W. Yin, Y. Zhuo, F. Kiani, B. Chen, X. Jiang *et al.*, Thousands of conductance levels in memristors integrated on CMOS, Nature (London) **615**, 823 (2023).

[8] E. M. Izhikevich, Neural excitability, spiking and bursting, Int. J. Bifurc. Chaos Appl. Sci. Eng. **10**, 1171 (2000).

[9] R.-M. Memmesheimer and M. Timme, Designing the dynamics of spiking neural networks, Phys. Rev. Lett. **97**, 188101 (2006).

[10] A. M. Yacomotti, P. Monnier, F. Raineri, B. B. Bakir, C. Seassal, R. Raj, and J. A. Levenson, Fast thermo-optical excitability in a two-dimensional photonic crystal, Phys. Rev. Lett. **97**, 143904 (2006).

[11] W. Coomans, L. Gelens, S. Beri, J. Danckaert, and G. Van der Sande, Solitary and coupled semiconductor ring lasers as optical spiking neurons, Phys. Rev. E **84**, 036209 (2011).

[12] M. Brunstein, A. M. Yacomotti, I. Sagnes, F. Raineri, L. Bigot, and A. Levenson, Excitability and self-pulsing in a photonic crystal nanocavity, Phys. Rev. A **85**, 031803(R) (2012).
[13] T. V. Vaerenbergh, M. Fiers, P. Mechet, T. Spuesens, R. Kumar, G. Morthier, B. Schrauwen, J. Dambre, and P. Bienstman, Cascadable excitability in microrings, Opt. Express **20**, 20292 (2012).
[14] F. Selmi, R. Braive, G. Beaudoin, I. Sagnes, R. Kuszelewicz, and S. Barbay, Relative refractory period in an excitable semiconductor laser, Phys. Rev. Lett. **112**, 183902 (2014).
[15] A. Sengupta, A. Banerjee, and K. Roy, Hybrid spintronic-CMOS spiking neural network with on-chip learning: Devices, circuits, and systems, Phys. Rev. Appl. **6**, 064003 (2016).
[16] P. R. Prucnal, B. J. Shastri, T. F. de Lima, M. A. Nahmias, and A. N. Tait, Recent progress in semiconductor excitable lasers for photonic spike processing, Adv. Opt. Photon. **8**, 228 (2016).
[17] J. M. Shainline, S. M. Buckley, R. P. Mirin, and S. W. Nam, Superconducting optoelectronic circuits for neuromorphic computing, Phys. Rev. Appl. **7**, 034013 (2017).
[18] R. Khymyn, I. Lisenkov, J. Voorheis, O. Sulymenko, O. Prokopenko, V. Tiberkevich, J. Akerman, and A. Slavin, Ultra-fast artificial neuron: Generation of picosecond-duration spikes in a current-driven antiferromagnetic auto-oscillator, Sci. Rep. **8**, 15727 (2018).
[19] A. N. Tait, T. Ferreira de Lima, M. A. Nahmias, H. B. Miller, H.-T. Peng, B. J. Shastri, and P. R. Prucnal, Silicon photonic modulator neuron, Phys. Rev. Appl. **11**, 064043 (2019).
[20] L. De Marinis, M. Cococcioni, P. Castoldi, and N. Andriolli, Photonic neural networks: A survey, IEEE Access **7**, 175827 (2019).
[21] A. Chakravarty, J. H. Mentink, C. S. Davies, K. T. Yamada, A. V. Kimel, and Th. Rasing, Supervised learning of an opto-magnetic neural network with ultrashort laser pulses, Appl. Phys. Lett. **114**, 192407 (2019).
[22] M. L. Schneider, C. A. Donnelly, I. W. Haygood, A. Wynn, S. E. Russek, M. A. Castellanos-Beltran, P. D. Dresselhaus, P. F. Hopkins, M. R. Pufall, and W. H. Rippard, Synaptic weighting in single flux quantum neuromorphic computing, Sci. Rep. **10**, 934 (2020).
[23] C. S. Dunham, S. Lilak, J. Hochstetter, A. Loeffler, R. Zhu, C. Chase, A. Z. Stieg, Z. Kuncic, and J. K. Gimzewski, Nanoscale neuromorphic networks and criticality: A perspective, J. Phys. Complex. **2**, 042001 (2021).
[24] M. Hejda, J. A. Alanis, I. Ortega-Piwonka, J. Lourenço, J. Figueiredo, J. Javaloyes, B. Romeira, and A. Hurtado, Resonant tunneling diode nano-optoelectronic excitable nodes for neuromorphic spike-based information processing, Phys. Rev. Appl. **17**, 024072 (2022).
[25] T. Mei and C. Q. Chen, In-memory mechanical computing, Nat. Commun. **14**, 5204 (2023).
[26] S. Slesazeck and T. Mikolajick, Nanoscale resistive switching memory devices: A review, Nanotechnology **30**, 352003 (2019).
[27] S. Prosandeev, J. Grollier, D. Talbayev, B. Dkhil, and L. Bellaiche, Ultrafast neuromorphic dynamics using hidden phases in the prototype of relaxor ferroelectrics, Phys. Rev. Lett. **126**, 027602 (2021).
[28] Y. Wei, G. Vats, and B. Noheda, Synaptic behaviour in ferroelectric epitaxial rhombohedral $Hf_{0.5}Zr_{0.5}O_2$ thin films, Neuromorph. Comput. Eng. **2**, 044007 (2022).
[29] Y. Zhai, P. Xie, J. Hu, X. Chen, Z. Feng, Z. Lv, G. Ding, K. Zhou, Y. Zhou, and S.-T. Han, Reconfigurable 2D-ferroelectric platform for neuromorphic computing, Appl. Phys. Rev. **10**, 011408 (2023).
[30] I. Chakraborty, G. Saha, and K. Roy, Photonic in-memory computing primitive for spiking neural networks using phase-change materials, Phys. Rev. Appl. **11**, 014063 (2019).
[31] B. Zhao and J. Ravichandran, Low-power microwave relaxation oscillators based on phase-change oxides for neuromorphic computing, Phys. Rev. Appl. **11**, 014020 (2019).
[32] V. Joshi, M. Le Gallo, S. Haefeli, I. Boybat, S. R. Nandakumar, C. Piveteau, M. Dazzi, B. Rajendran, A. Sebastian, and E. Eleftheriou, Accurate deep neural network inference using computational phase-change memory, Nat. Commun. **11**, 2473 (2020).
[33] L. Sun, Y. Zhang, G. Han, G. Hwang, J. Jiang, B. Joo, K. Watanabe, T. Taniguchi, Y.-M. Kim, W. J. Yu, B.-S. Kong, R. Zhao, and H. Yang, Self-selective van der Waals heterostructures for large scale memory array, Nat. Commun. **10**, 3161 (2019).
[34] L. Mennel, J. Symonowicz, S. Wachter, D. K. Polyushkin, A. J. Molina-Mendoza, and T. Mueller, Ultrafast machine vision with 2D material neural network image sensors, Nature (London) **579**, 62 (2020).
[35] Y. van de Burgt, E. Lubberman, E. J. Fuller, S. T. Keene, G. C. Faria, S. Agarwal, M. J. Marinella, A. Alec Talin, and A. Salleo, A non-volatile organic electrochemical device as a low-voltage artificial synapse for neuromorphic computing, Nat. Mater. **16**, 414 (2017).
[36] S. Satapathi, K. Raj, Yukta, and M. A. Afroz, Halide-perovskite-based memristor devices and their application in neuromorphic computing, Phys. Rev. Appl. **18**, 017001 (2022).
[37] D. E. Chang, V. Vuletić, and M. D. Lukin, Quantum nonlinear optics—Photon by photon, Nat. Photon. **8**, 685 (2014).
[38] E. Togan, H.-T. Lim, S. Faelt, W. Wegscheider, and A. Imamoglu, Enhanced interactions between dipolar polaritons, Phys. Rev. Lett. **121**, 227402 (2018).
[39] E. Estrecho, T. Gao, N. Bobrovska, D. Comber-Todd, M. D. Fraser, M. Steger, K. West, L. N. Pfeiffer, J. Levinsen, M. M. Parish, T. C. H. Liew, M. Matuszewski, D. W. Snoke, A. G. Truscott, and E. A. Ostrovskaya, Direct measurement of polariton-polariton interaction strength in the Thomas-Fermi regime of exciton-polariton condensation, Phys. Rev. B **100**, 035306 (2019).
[40] S. A. Mann, N. Nookala, S. C. Johnson, M. Cotrufo, A. Mekawy, J. F. Klem, I. Brener, M. B. Raschke, A. Alù, and M. A. Belkin, Ultrafast optical switching and power limiting in intersubband polaritonic metasurfaces, Optica **8**, 606 (2021).
[41] J. B. Khurgin, Nonlinear optics from the viewpoint of interaction time, Nat. Photon. **17**, 545 (2023).
[42] C. Haldeman and J. M. Beggs, Critical branching captures activity in living neural networks and maximizes the number of metastable states, Phys. Rev. Lett. **94**, 058101 (2005).
[43] N. Friedman, S. Ito, B. A. W. Brinkman, M. Shimono, R. E. Lee DeVille, K. A. Dahmen, J. M. Beggs, and T. C.

Butler, Universal critical dynamics in high resolution neuronal avalanche data, Phys. Rev. Lett. **108**, 208102 (2012).
[44] S. di Santo, R. Burioni, A. Vezzani, and M. A. Muñoz, Self-organized bistability associated with first-order phase transitions, Phys. Rev. Lett. **116**, 240601 (2016).
[45] M. A. Muñoz, Colloquium: Criticality and dynamical scaling in living systems, Rev. Mod. Phys. **90**, 031001 (2018).
[46] V. Buendía, S. di Santo, P. Villegas, R. Burioni, and M. A. Muñoz, Self-organized bistability and its possible relevance for brain dynamics, Phys. Rev. Res. **2**, 013318 (2020).
[47] D. Plenz, T. L. Ribeiro, S. R. Miller, P. A. Kells, A. Vakili, and E. L. Capek, Self-organized criticality in the brain, Front. Phys. **9**, 639389 (2021).
[48] J. O'Byrne and K. Jerbi, How critical is brain criticality? Trends Neurosci. **45**, 820 (2022).
[49] C. G. Langton, Computation at the edge of chaos: Phase transitions and emergent computation, Physica D **42**, 12 (1990).
[50] N. Bertschinger and T. Natschläger, Real-time computation at the edge of chaos in recurrent neural networks, Neural Comput. **16**, 1413 (2004).
[51] J. Boedecker, O. Obst, J. T. Lizier, N. M. Mayer, and M. Asada, Information processing in echo state networks at the edge of chaos, Theory Biosci. **131**, 205 (2012).
[52] B. Cramer, D. Stöckel, M. Kreft, M. Wibral, J. Schemmel, K. Meier, and V. Priesemann, Control of criticality and computation in spiking neuromorphic networks with plasticity, Nat. Commun. **11**, 2853 (2020).
[53] J. Hochstetter, R. Zhu, A. Loeffler, A. Diaz-Alvarez, T. Nakayama, and Z. Kuncic, Avalanches and edge-of-chaos learning in neuromorphic nanowire networks, Nat. Commun. **12**, 4008 (2021).
[54] A. Borst and F. E. Theunissen, Information theory and neural coding, Nat. Neurosci. **2**, 947 (1999).
[55] M. Diesmann, M.-O. Gewaltig, and A. Aertsen, Stable propagation of synchronous spiking in cortical neural networks, Nature (London) **402**, 529 (1999).
[56] A. Kumar, S. Rotter, and A. Aertsen, Spiking activity propagation in neuronal networks: Reconciling different perspectives on neural coding, Nat. Rev. Neurosci. **11**, 615 (2010).
[57] D. Sihn and S.-P. Kim, A spike train distance robust to firing rate changes based on the earth mover's distance, Front. Comput. Neurosci. **13**, 82 (2019).
[58] Y.-J. Lee, M. B. On, X. Xiao, R. Proietti, and S. J. B. Yoo, Photonic spiking neural networks with event-driven femtojoule optoelectronic neurons based on Izhikevich-inspired model, Opt. Express **30**, 19360 (2022).
[59] F. Marino, G. Catalán, P. Sánchez, S. Balle, and O. Piro, Thermo-optical "canard orbits" and excitable limit cycles, Phys. Rev. Lett. **92**, 073901 (2004).
[60] P. Z. G. Fonseca, I. Alda, F. Marino, A. Cuadrado, V. D'Ambrosio, J. Gieseler, and R. Quidant, Slow thermo-optomechanical pulsations in suspended one-dimensional photonic crystal nanocavities, Phys. Rev. A **102**, 053518 (2020).
[61] Z. Geng, K. J. H. Peters, A. A. P. Trichet, K. Malmir, R. Kolkowski, J. Smith, and S. R. K. Rodriguez, Universal scaling in the dynamic hysteresis, and non-Markovian dynamics, of a tunable optical cavity, Phys. Rev. Lett. **124**, 153603 (2020).
[62] K. J. H. Peters, Z. Geng, K. Malmir, J. M. Smith, and S. R. K. Rodriguez, Extremely broadband stochastic resonance of light and enhanced energy harvesting enabled by memory effects in the nonlinear response, Phys. Rev. Lett. **126**, 213901 (2021).
[63] V. R. Almeida and M. Lipson, Optical bistability on a silicon chip, Opt. Lett. **29**, 2387 (2004).
[64] G. Priem, P. Dumon, W. Bogaerts, D. V. Thourhout, G. Morthier, and R. Baets, Optical bistability and pulsating behaviour in silicon-on-insulator ring resonator structures, Opt. Express **13**, 9623 (2005).
[65] Y. Shi, X. Chen, F. Lou, Y. Chen, M. Yan, L. Wosinski, and M. Qiu, All-optical switching of silicon disk resonator based on photothermal effect in metal-insulator-metal absorber, Opt. Lett. **39**, 4431 (2014).
[66] T. Carmon, L. Yang, and K. J. Vahala, Dynamical thermal behavior and thermal self-stability of microcavities, Opt. Express **12**, 4742 (2004).
[67] M. Notomi, A. Shinya, S. Mitsugi, G. Kira, E. Kuramochi, and T. Tanabe, Optical bistable switching action of Si high-Q photonic-crystal nanocavities, Opt. Express **13**, 2678 (2005).
[68] M. Brunstein, R. Braive, R. Hostein, A. Beveratos, I. Robert-Philip, I. Sagnes, T. J. Karle, A. M. Yacomotti, J. A. Levenson, V. Moreau, G. Tessier, and Y. D. Wilde, Thermo-optical dynamics in an optically pumped photonic crystal nano-cavity, Opt. Express **17**, 17118 (2009).
[69] M. Sodagar, M. Miri, A. A. Eftekhar, and A. Adibi, Optical bistability in a one-dimensional photonic crystal resonator using a reverse-biased pn-junction, Opt. Express **23**, 2676 (2015).
[70] K. Perrier, S. Greveling, H. Wouters, S. R. K. Rodriguez, G. Lehoucq, S. Combrié, A. de Rossi, S. Faez, and A. P. Mosk, Thermo-optical dynamics of a nonlinear GaInP photonic crystal nanocavity depend on the optical mode profile, OSA Continuum **3**, 1879 (2020).
[71] J. B. Khurgin, G. Sun, W. T. Chen, W.-Y. Tsai, and D. P. Tsai, Ultrafast thermal nonlinearity, Sci. Rep. **5**, 17899 (2015).
[72] E. J. Doedel, B. E. Oldeman, A. R. Champneys, F. Dercole, T. F. Fairgrieve, Y. A. Kuznetsov, R. C. Paffenroth, B. Sandstede, X. Wang, and C. Zhang, AUTO-07P: Continuation and bifurcation software for ordinary differential equations, AUTO-07P software (2012).
[73] S. H. Strogatz, *Nonlinear Dynamics and Chaos: With Applications to Physics, Biology, Chemistry, and Engineering*, 2nd ed. (Taylor & Francis Ltd., London, 2018).
[74] P. D. Drummond and D. F. Walls, Quantum theory of optical bistability, I. Nonlinear polarisability model, J. Phys. A **13**, 725 (1980).
[75] M. Soljačić, M. Ibanescu, S. G. Johnson, Y. Fink, and J. D. Joannopoulos, Optimal bistable switching in nonlinear photonic crystals, Phys. Rev. E **66**, 055601(R) (2002).
[76] C. Khandekar, Z. Lin, and A. W. Rodriguez, Thermal radiation from optically driven Kerr ($\chi^{(3)}$) photonic cavities, Appl. Phys. Lett. **106**, 151109 (2015).
[77] W. Casteels, F. Storme, A. Le Boité, and C. Ciuti, Power laws in the dynamic hysteresis of quantum nonlinear photonic resonators, Phys. Rev. A **93**, 033824 (2016).
[78] S. R. K. Rodriguez, W. Casteels, F. Storme, N. Carlon Zambon, I. Sagnes, L. Le Gratiet, E. Galopin, A. Lemaître, A. Amo, C. Ciuti, and J. Bloch, Probing a dissipative phase

transition via dynamical optical hysteresis, Phys. Rev. Lett. **118**, 247402 (2017).
[79] W. Casteels, R. Fazio, and C. Ciuti, Critical dynamical properties of a first-order dissipative phase transition, Phys. Rev. A **95**, 012128 (2017).
[80] K. J. H. Peters and S. R. K. Rodriguez, Exceptional precision of a nonlinear optical sensor at a square-root singularity, Phys. Rev. Lett. **129**, 013901 (2022).
[81] B. Braeckeveldt and B. Maes, Temperature-induced stochastic resonance in Kerr photonic cavities for frequency shift, J. Opt. Soc. Am. B **39**, 2074 (2022).
[82] K. J. H. Peters, J. Busink, P. Ackermans, K. G. Cognée, and S. R. K. Rodriguez, Scalar potentials for light in a cavity, Phys. Rev. Res. **5**, 013154 (2023).
[83] K. Peters and S. Rodriguez, Limit cycles and chaos induced by a nonlinearity with memory, Eur. Phys. J. Spec. Top. **231**, 247 (2022).
[84] D. Sarkar, S. S. Gavrilov, M. Sich, J. H. Quilter, R. A. Bradley, N. A. Gippius, K. Guda, V. D. Kulakovskii, M. S. Skolnick, and D. N. Krizhanovskii, Polarization bistability and resultant spin rings in semiconductor microcavities, Phys. Rev. Lett. **105**, 216402 (2010).
[85] P. M. Walker, L. Tinkler, B. Royall, D. V. Skryabin, I. Farrer, D. A. Ritchie, M. S. Skolnick, and D. N. Krizhanovskii, Dark solitons in high velocity waveguide polariton fluids, Phys. Rev. Lett. **119**, 097403 (2017).
[86] P. Stepanov, I. Amelio, J.-G. Rousset, J. Bloch, A. Lemaître, A. Amo, A. Minguzzi, I. Carusotto, and M. Richard, Dispersion relation of the collective excitations in a resonantly driven polariton fluid, Nat. Commun. **10**, 3869 (2019).
[87] I. Amelio, A. Minguzzi, M. Richard, and I. Carusotto, Galilean boosts and superfluidity of resonantly driven polariton fluids in the presence of an incoherent reservoir, Phys. Rev. Res. **2**, 023158 (2020).
[88] A. M. Grudinina and N. S. Voronova, Dark and thermal reservoir contributions to polariton sound velocity, Phys. Rev. B **106**, L121301 (2022).
[89] D. Schmidt, B. Berger, M. Kahlert, M. Bayer, C. Schneider, S. Höfling, E. S. Sedov, A. V. Kavokin, and M. Aßmann, Tracking dark excitons with exciton polaritons in semiconductor microcavities, Phys. Rev. Lett. **122**, 047403 (2019).
[90] P. Hamel, S. Haddadi, F. Raineri, P. Monnier, G. Beaudoin, I. Sagnes, A. Levenson, and A. M. Yacomotti, Spontaneous mirror-symmetry breaking in coupled photonic-crystal nanolasers, Nat. Photon. **9**, 311 (2015).
[91] B. Garbin, A. Giraldo, K. J. H. Peters, N. G. R. Broderick, A. Spakman, F. Raineri, A. Levenson, S. R. K. Rodriguez, B. Krauskopf, and A. M. Yacomotti, Spontaneous symmetry breaking in a coherently driven nanophotonic Bose-Hubbard dimer, Phys. Rev. Lett. **128**, 053901 (2022).
[92] B. Peng, Ş. K. Özdemir, F. Lei, F. Monifi, M. Gianfreda, G. L. Long, S. Fan, F. Nori, C. M. Bender, and L. Yang, Parity–time-symmetric whispering-gallery microcavities, Nat. Phys. **10**, 394 (2014).
[93] S. R. K. Rodriguez, A. Amo, I. Sagnes, L. Le Gratiet, E. Galopin, A. Lemaître, and J. Bloch, Interaction-induced hopping phase in driven-dissipative coupled photonic microcavities, Nat. Commun. **7**, 11887 (2016).
[94] N. Carlon Zambon, S. R. K. Rodriguez, A. Lemaître, A. Harouri, L. Le Gratiet, I. Sagnes, P. St-Jean, S. Ravets, A. Amo, and J. Bloch, Parametric instability in coupled nonlinear microcavities, Phys. Rev. A **102**, 023526 (2020).
[95] S. Dufferwiel, F. Li, A. A. P. Trichet, L. Giriunas, P. M. Walker, I. Farrer, D. A. Ritchie, J. M. Smith, M. S. Skolnick, and D. N. Krizhanovskii, Tunable polaritonic molecules in an open microcavity system, Appl. Phys. Lett. **107**, 201106 (2015).
[96] C. Kurtscheid, D. Dung, E. Busley, F. Vewinger, A. Rosch, and M. Weitz, Thermally condensing photons into a coherently split state of light, Science **366**, 894 (2019).
[97] C. Toebes, M. Vretenar, and J. Klaers, Dispersive and dissipative coupling of photon Bose-Einstein condensates, Commun. Phys. **5**, 59 (2022).
[98] V. Ardizzone, P. Lewandowski, M.-H. Luk, Y.-C. Tse, N.-H. Kwong, A. Lücke, M. Abbarchi, E. Baudin, E. Galopin, J. Bloch *et al.*, Formation and control of turing patterns in a coherent quantum fluid, Sci. Rep. **3**, 3016 (2013).
[99] G. Xu, A. U. Nielsen, B. Garbin, L. Hill, G.-L. Oppo, J. Fatome, S. G. Murdoch, S. Coen, and M. Erkintalo, Spontaneous symmetry breaking of dissipative optical solitons in a two-component Kerr resonator, Nat. Commun. **12**, 4023 (2021).
[100] B. Maes, M. Soljačić, J. D. Joannopoulos, P. Bienstman, R. Baets, S.-P. Gorza, and M. Haelterman, Switching through symmetry breaking in coupled nonlinear micro-cavities, Opt. Express **14**, 10678 (2006).
[101] D. Sarchi, I. Carusotto, M. Wouters, and V. Savona, Coherent dynamics and parametric instabilities of microcavity polaritons in double-well systems, Phys. Rev. B **77**, 125324 (2008).
[102] B. Maes, M. Fiers, and P. Bienstman, Self-pulsing and chaos in short chains of coupled nonlinear microcavities, Phys. Rev. A **80**, 033805 (2009).
[103] I. Hendry, W. Chen, Y. Wang, B. Garbin, J. Javaloyes, G.-L. Oppo, S. Coen, S. G. Murdoch, and M. Erkintalo, Spontaneous symmetry breaking and trapping of temporal Kerr cavity solitons by pulsed or amplitude-modulated driving fields, Phys. Rev. A **97**, 053834 (2018).
[104] A. U. Nielsen, B. Garbin, S. Coen, S. G. Murdoch, and M. Erkintalo, Coexistence and interactions between nonlinear states with different polarizations in a monochromatically driven passive Kerr resonator, Phys. Rev. Lett. **123**, 013902 (2019).
[105] A. Giraldo, B. Krauskopf, N. G. R. Broderick, J. A. Levenson, and A. M. Yacomotti, The driven-dissipative Bose–Hubbard dimer: Phase diagram and chaos, New J. Phys. **22**, 043009 (2020).
[106] J. Yelo-Sarrión, P. Parra-Rivas, N. Englebert, C. M. Arabí, F. Leo, and S.-P. Gorza, Self-pulsing in driven-dissipative photonic Bose-Hubbard dimers, Phys. Rev. Res. **3**, L042031 (2021).
[107] J. Yelo-Sarrión, F. Leo, S.-P. Gorza, and P. Parra-Rivas, Self-pulsing and chaos in the asymmetrically driven dissipative photonic Bose–Hubbard dimer: A bifurcation analysis, Chaos **32**, 083103 (2022).
[108] J. Yelo-Sarrión, F. Leo, S.-P. Gorza, and P. Parra-Rivas, Neuronlike spiking dynamics in asymmetrically driven dissipative nonlinear photonic dimers, Phys. Rev. A **106**, 013512 (2022).

[109] B. Braeckeveldt and B. Maes, Thermal radiation in asymmetrically driven coupled non-linear photonic cavities, Phys. Rev. B **107**, 174310 (2023).

[110] T. L. Heugel, A. Eichler, R. Chitra, and O. Zilberberg, The role of fluctuations in quantum and classical time crystals, SciPost Phys. Core **6**, 053 (2023).

[111] B. Cao, K. W. Mahmud, and M. Hafezi, Two coupled nonlinear cavities in a driven-dissipative environment, Phys. Rev. A **94**, 063805 (2016).

[112] G. E. Ha and E. Cheong, Spike frequency adaptation in neurons of the central nervous system, Exp. Neurobiol. **26**, 179 (2017).

[113] J. Benda and A. V. M. Herz, A universal model for spike-frequency adaptation, Neural Comput. **15**, 2523 (2003).

[114] B. A. Malomed, *Spontaneous Symmetry Breaking, Self-Trapping, and Josephson Oscillations* (Springer, New York, 2013).

[115] Q.-T. Cao, H. Wang, C.-H. Dong, H. Jing, R.-S. Liu, X. Chen, L. Ge, Q. Gong, and Y.-F. Xiao, Experimental demonstration of spontaneous chirality in a nonlinear microresonator, Phys. Rev. Lett. **118**, 033901 (2017).

[116] B. Garbin, J. Fatome, G.-L. Oppo, M. Erkintalo, S. G. Murdoch, and S. Coen, Asymmetric balance in symmetry breaking, Phys. Rev. Res. **2**, 023244 (2020).

[117] A. Krasnok and A. Alù, Low-symmetry nanophotonics, ACS Photon. **9**, 2 (2022).

[118] L. Hill, G.-L. Oppo, and P. Del'Haye, Multi-stage spontaneous symmetry breaking of light in Kerr ring resonators, Commun. Phys. **6**, 208 (2023).

[119] M. Desroches, B. Krauskopf, and H. M. Osinga, Numerical continuation of canard orbits in slow–fast dynamical systems, Nonlinearity **23**, 739 (2010).

[120] J. Wen, H. Zhang, Z. Wu, Q. Wang, H. Yu, W. Sun, B. Liang, C. He, K. Xiong, Y. Pan, Y. Zhang, and Z. Liu, All-optical spiking neural network and optical spike-time-dependent plasticity based on the self-pulsing effect within a micro-ring resonator, Appl. Opt. **62**, 5459 (2023).